

# Modeling Atomic-Scale Electrical Contact Quality Across Two-Dimensional Interfaces

Aisheng Song,<sup>†</sup> Ruoyu Shi,<sup>†</sup> Hongliang Lu,<sup>‡,§</sup> Lei Gao,<sup>||</sup> Qunyang Li,<sup>†,⊥</sup> Hui Guo,<sup>‡,§</sup> Yanmin Liu,<sup>†</sup> Jie Zhang,<sup>†</sup> Yuan Ma,<sup>||</sup> Xin Tang,<sup>†</sup> Shixuan Du,<sup>‡,§</sup> Xin Li,<sup>#</sup> Xiao Liu,<sup>†</sup> Yuan-Zhong Hu,<sup>†</sup> Hong-Jun Gao,<sup>‡,§</sup> Jianbin Luo,<sup>†</sup> and Tian-Bao Ma<sup>\*,†</sup>

<sup>†</sup>State Key Laboratory of Tribology, Tsinghua University, Beijing 100084, China

<sup>‡</sup>School of Physical Sciences, University of Chinese Academy of Sciences, Beijing 100049, China

<sup>§</sup>Institute of Physics, Chinese Academy of Sciences, Beijing 100190, China

<sup>||</sup>Beijing Advanced Innovation Center for Materials Genome Engineering, Institute for Advanced Materials and Technology, University of Science and Technology Beijing, Beijing 100083, China

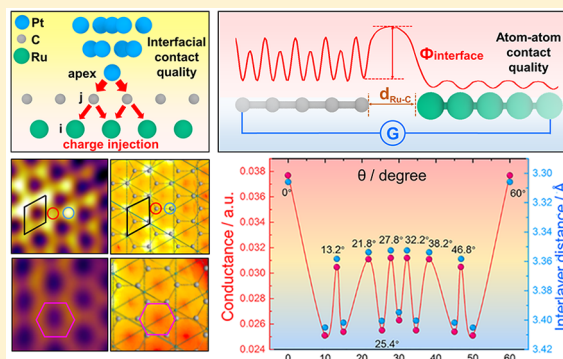
<sup>⊥</sup>AML, CNMM, School of Aerospace Engineering, Tsinghua University, Beijing 100084, China

<sup>#</sup>Laser Micro/Nano Fabrication Laboratory, School of Mechanical Engineering, Beijing Institute of Technology, Beijing 100081, China

## Supporting Information

**ABSTRACT:** Contacting interfaces with physical isolation and weak interactions usually act as barriers for electrical conduction. The electrical contact conductance across interfaces has long been correlated with the true contact area or the “contact quantity”. Much of the physical understanding of the interfacial electrical contact quality was primarily based on Landauer’s theory or Richardson formulation. However, a quantitative model directly connecting contact conductance to interfacial atomistic structures still remains absent. Here, we measure the atomic-scale local electrical contact conductance instead of local electronic surface states in graphene/Ru(0001) superstructure, via atomically resolved conductive atomic force microscopy. By defining the “quality” of individual atom–atom contact as the carrier tunneling probability along the interatomic electron transport pathways, we establish a relationship between the atomic-scale contact quality and local interfacial atomistic structure. This real-space model unravels the atomic-level spatial modulation of contact conductance, and the twist angle-dependent interlayer conductance between misoriented graphene layers.

**KEYWORDS:** Two-dimensional materials, heterostructure, electrical contacts, atomic resolution imaging, *ab initio* calculations, real-space model



The resistance of electrical transport across the contacting interfaces has long been a critical issue for applications where the transmission efficiency and reliability of electrical energy and signals are highly demanded.<sup>1,2</sup> It has been elucidated that the interfacial contact conductance strongly depends on the “contact quantity”, that is, the true contact area, for both multiasperity contacts between rough surfaces<sup>3–5</sup> and atomic-sized ballistic contacts through which the current flows.<sup>6–8</sup> On the other hand, among many applications, the electrical contact conductance between two-dimensional (2D) materials and metals, or 2D/2D material layers, is of fundamental importance in high-performance device applications,<sup>1,2,9–12</sup> which strongly depend on the interfacial contact quality. The contact quality has been reported to be highly dependent on the electron transmission probability or electrostatic barrier across the interface,<sup>1,9,13,14</sup> which has

been successfully modeled by Landauer’s theory or Richardson formulation.<sup>1,14–18</sup> However, a real-space model which directly connects electrical contact quality to interfacial atomistic structures still remains absent.

Experimentally, the interfacial contact conductance was reflected by the device-level transport measurements.<sup>14,19–22</sup> Recently, conductive atomic force microscopy (c-AFM), a powerful tool for measuring conductance on nanoscale,<sup>23</sup> was adopted to study the twist angle dependence of interfacial conductance between MoS<sub>2</sub>/graphene heterojunction.<sup>16</sup> These results indicate the “averaged” contact quality across the interface. Scanning tunneling microscopy by measuring the

Received: February 17, 2019

Revised: May 7, 2019

Published: May 15, 2019

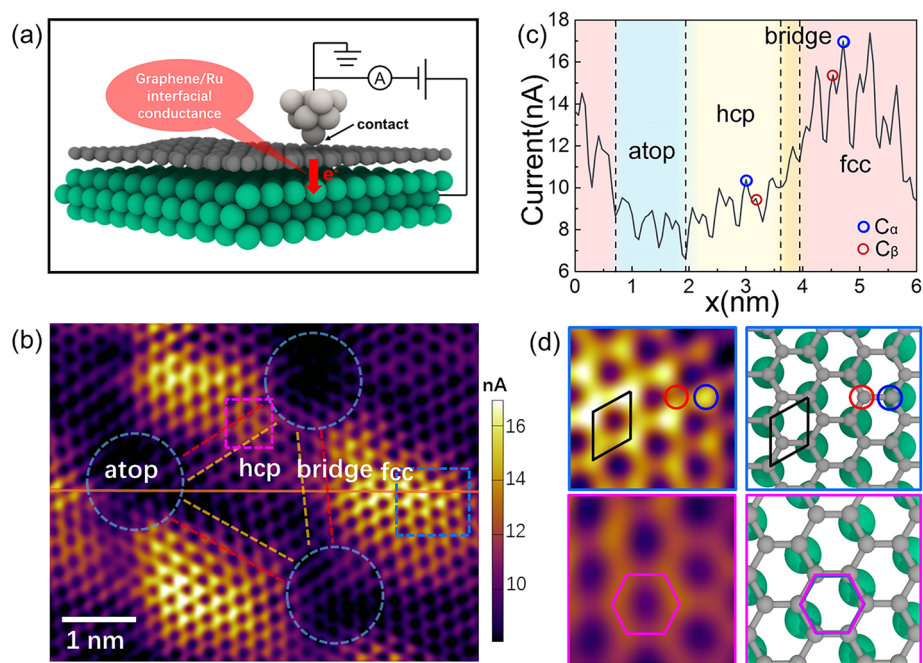


**Figure 1.** Local current/conductance measurement using atomically resolved c-AFM. (a) Schematic diagram of c-AFM measurement. (b) Atomistic resolution local current map of graphene/Ru(0001) measured at bias voltage = 20 mV, normal load = 1000 nN (details in [Materials and Methods](#)). It is a local enlargement of the experimental result with a very small rotation angle for a clearer expression. The original maps are shown in [Figure S4](#). (c) Profile of current map along the orange line in panel b. (d) Local enlargement of fcc region (blue square) and bridge region (pink square) in panel b as well as the corresponding atomic configurations. The blue and red circles represent  $C_\alpha$  and  $C_\beta$ , respectively.

tip-sample tunneling current has been widely adopted to study the moiré superlattice level and atomic-level modulation of local density of states of graphene by the metal substrates.<sup>24–28</sup> However, a direct measurement of interfacial conductance between 2D materials and underlying substrates with atomic resolution is still lacking. These hinder the quantitative description of the atomic-scale electrical contact quality and rational design of the local interfacial atomistic structures toward a better contact performance.<sup>29</sup>

The relationship between the contact quality and atomistic configurations of sliding interfaces has been studied historically in the context of friction.<sup>29,30</sup> Through investigating the evolution of frictional contact quality (the local pinning state of individual atoms as well as the atomic alignment of the interface), the experimental observations of layer-dependent friction and frictional strengthening effects of configurationally flexible graphene on a loosely adhering substrate were well understood.<sup>29,31</sup> Here, a combined atomically resolved c-AFM measurement, density functional theory (DFT), and non-equilibrium Green's function (NEGF) calculation have been conducted to unravel the atomic-scale mechanism of interfacial electron transport. A theoretical model has been derived to describe the relationship between the electrical contact quality and interfacial atomistic structures in 2D material/metal and 2D/2D material contacts, which is further adopted to describe the atomic-level spatial modulation of contact conductance and the angular dependence of interlayer conductance between misoriented graphene layers.

By scanning a conductive AFM tip under the contact mode ([Figure 1a](#)), we were able to measure with atomic resolution the spatial distribution of current flowing through the tip/graphene/Ru junction (a quantity that scales with local conductance), as shown in [Figure 1b](#). Although the measurement was done in atmospheric environment, the general

influencing factors of water and external molecules adsorption on graphene surfaces impose limited effects on the c-AFM measurement<sup>32–34</sup> ([Figure S1](#), [Supplementary Discussion 1](#) in [Supporting Information](#)). The current image shows a moiré superlattice level modulation, indicating a larger local conductance in the face-centered cubic (fcc), bridge, and hexagonal close-packed (hcp) regions than in the bowed-up atop regions ([Figure 1b](#), [Figure S2](#)), where fcc, hcp, atop, and bridge are the regions in which the location of hexagonal holes of the graphene layer are on the fcc hollow, hcp hollow, top, and bridge sites of the Ru atoms in the first layer of the Ru(0001) substrate, respectively. Interestingly, an atomic-level contrast in local conductance could also be clearly distinguished as  $C_\alpha$  (blue circle) and  $C_\beta$  (red circle) sites, especially in the fcc and hcp regions as shown in [Figure 1c,d](#). The local contact conductance at  $C_\alpha$  is roughly 15% higher than at  $C_\beta$  site. We find that this contrast coincides with the variation in the local stacking geometry between graphene and Ru(0001) substrate. The locations of the stronger current peaks ( $C_\alpha$ ) correspond to the carbon atoms sitting above the Ru atom in the topmost layer, whereas the weaker current peaks ( $C_\beta$ ) correspond to the carbon atoms sitting above the vacancies of the topmost Ru layer. The contrast is invisible for carbon atoms in the bridge region, which are geometrically equivalent with regard to the underlying Ru atom. These results suggest that the interfacial stacking geometry between graphene and Ru(0001) substrate has imposed great influence on the atomic-scale local conductance, which is enhanced at the fcc/hcp region (and  $C_\alpha > C_\beta$ ) and suppressed at the atop region. It has been extensively demonstrated by scanning tunneling microscopy (STM) that metal substrates could substantially modulate the electronic states of the graphene overlayer.<sup>24–27</sup> However, the c-AFM result here is significantly different from the reported STM results ([Figure S3](#) and

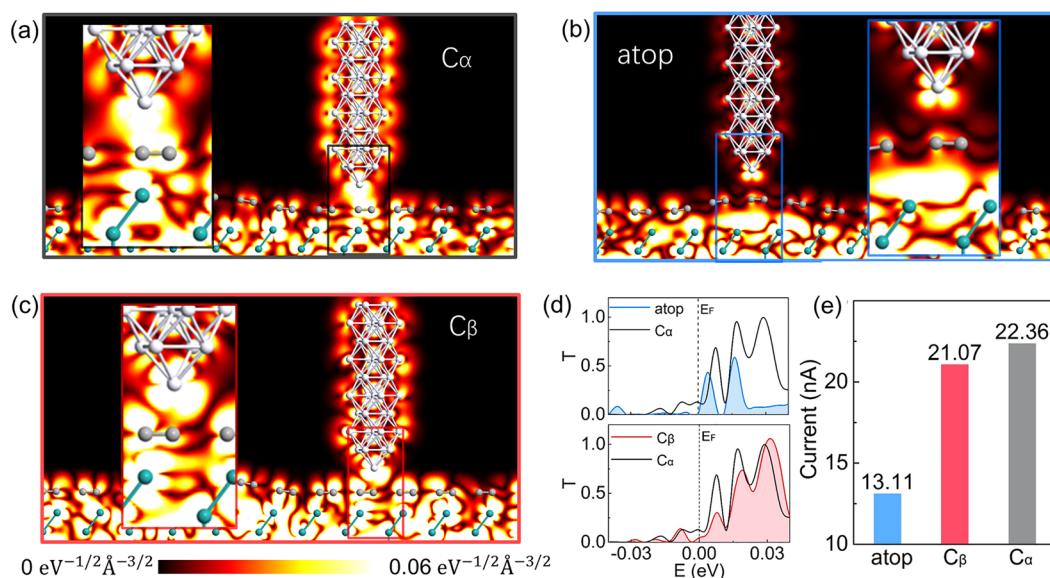


**Figure 2.** Electronic transport properties across the electrode/graphene/Ru junctions. (a–c) Transmission eigenstates at  $E_F$  when the tip is right above  $C_\alpha$ ,  $C_\beta$ , and atop positions, indicating the amplitudes of scattering states traveling through the interface. (d) Transmission spectra of atop,  $C_\alpha$ , and  $C_\beta$  containing the transmission coefficients  $T$  at energy  $E$  in the range  $E_F - 0.04 \text{ eV} < E < E_F + 0.04 \text{ eV}$ . (e) Calculated current (electrical conductance) when the Pt electrode is placed at  $C_\alpha$ ,  $C_\beta$ , and atop positions with 1 mV bias voltage.

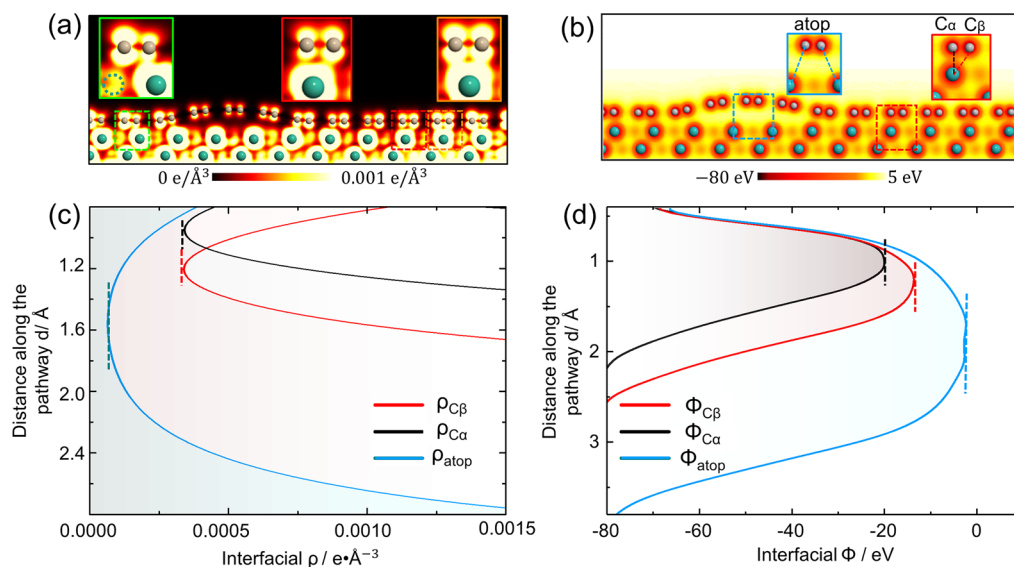


**Figure 3.** Electronic states and tunneling barrier at graphene/Ru(0001) interface. (a) Density of charge carriers ( $\rho$ ) corresponding to the electronic states within the energy range  $E_F - 0.1 \text{ eV} < E < E_F + 0.1 \text{ eV}$ , in the plane normal to the interface along the orange line in Figure 1b. (b) Electrostatic potential ( $\Phi$ ) distribution in the plane normal to the interface. (c,d) The line profiles of  $\rho$  and  $\Phi$  along the electronic transport pathways indicated by the dashed lines in (b).

Supplementary Discussion 2 in Supporting Information) and cannot be explained and modeled by existing theories.<sup>25–28</sup> The possible reason could be that STM images mainly reflect the local surface states of the samples, while the c-AFM results are more indicative of the graphene/Ru interfacial transport properties.

NEGF based electronic transport calculations have been conducted to reveal the mechanism of the contrast in local interfacial conductance.<sup>35,36</sup> The conductance should depend on the contact geometries of both the tip–graphene and graphene–Ru interfaces. Because graphene is strongly bound to the Ru substrate, the alignment between tip and graphene layer was suppressed in the present system.<sup>29</sup> Therefore, the

alignment between the tip and graphene layer here plays a less significant role in determining the interfacial contact quality. Also subject to the expensive computational cost of both DFT and NEGF calculations, a simplified 10-Pt-atom tip model instead of an actual tip with finite size was positioned with constant distance above the characteristic carbon atoms ( $C_\alpha$ ,  $C_\beta$ , and atop, respectively) to qualitatively analyze the local transport properties at the atomic scale (see Figure S5 for detailed simulation model).<sup>37</sup> The transmission eigenstates shown in Figure 2a–c represent the Fermi-energy ( $E_F$ ) scattering states traveling through the graphene/Ru interface, possessing the most continuous orbital at the interface and the largest amplitude at the upper electrode when the electrode is

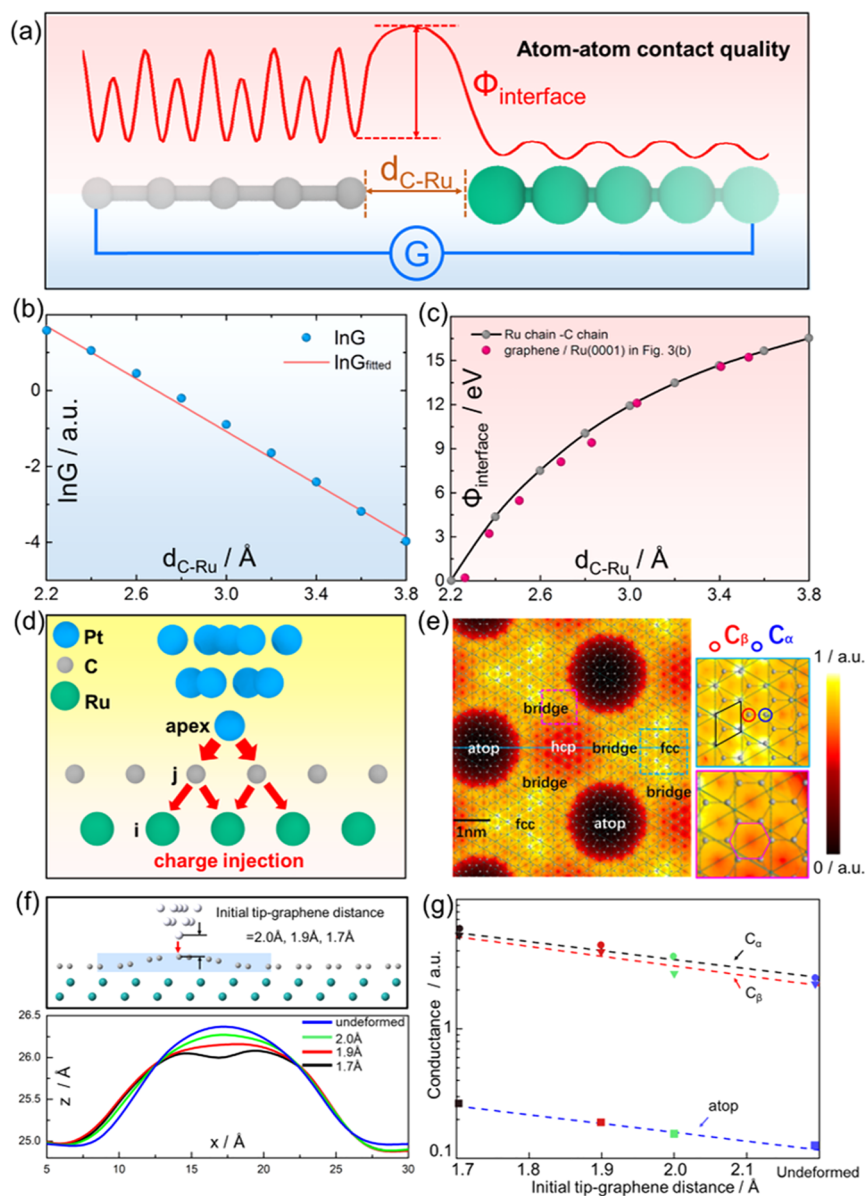


**Figure 4.** A model for calculating the conductance of 2D interfaces by considering individual atom–atom “contact quality”. (a) Ru chain–C chain contact model for calculating individual atom–atom contact conductance  $G_{\text{atomic}}$  and  $\Phi$  of interatomic transport pathway. (b)  $G_{\text{atomic}}(d_{\text{C-Ru}})$  calculated using DFT+NEGF at the bias voltage of 0.1 V. (c)  $\Phi(d_{\text{C-Ru}})$  calculated by Ru chain–C chain model (black curve) and compared with the  $\Phi$  calculated by graphene/Ru(0001) model as shown in Figure 3b (red dots). The minimum barrier height is set as zero point. (d) Schematic diagram of the model for simulating c-AFM, where the Pt atom represents the c-AFM tip. Electrons are transported along the interatomic pathways with different transfer efficiency, corresponding to different atom–atom contact quality. (e) Simulation result of the c-AFM atomistic resolution local conductance map. (f) The schematic of the indentation process of a 10 Pt atoms tip on the graphene at atop region to simulate the deformations of graphene under different contact loads, and the profiles of deformed graphene calculated by DFT. (g) The local electrical conductance of deformed graphene calculated by our ACQ model.

positioned on top of  $C_\alpha$  atom shown in Figure 2a, as compared to that on top of atop and  $C_\beta$  atoms shown in Figure 2b,c). This is consistent with the comparison of transmission coefficients at the Fermi-energy  $T_{C_\alpha} > T_{C_\beta} > T_{\text{atop}}$  in Figure 2d, the calculated local current under 1 mV bias voltage  $I_{C_\alpha} > I_{C_\beta} > I_{\text{atop}}$  in Figure 2e, and the c-AFM results in Figure 1c,d, indicating the highest carrier tunneling probability or best “contact quality” at  $C_\alpha$  position. The agreement of numerical simulations and experimental measurements also indicates that the contrast of local conductance at atop,  $C_\alpha$ , and  $C_\beta$  positions is primarily induced by the atomic alignment between graphene and Ru substrate.

In order to unravel the physical mechanism of the interfacial carrier tunneling behavior and its dependence on local atomic configuration, the availability of electronic states around the Fermi-energy and the efficiency of carrier tunneling were characterized in Figure 3. As shown by the charge carrier density ( $\rho$ ) distribution in Figure 3a and insets therein, the interfacial charge carriers concentrate predominantly in the space between C and underlying Ru atoms, suggesting that the easiest pathways for interfacial electronic transport are through the straight lines between individual C–Ru pair atoms. The transport pathways were explicitly indicated together with the electrostatic potential ( $\Phi$ ) distribution in Figure 3b and the

insets therein. The carrier density profiles along the interfacial transport pathways shown in Figure 3c, as well as the local density of states (LDOS) of the system (Figure S6), signify the availability of corresponding electronic states. The maximum values of the electrostatic potential profiles along the same transport pathways in Figure 3d represents the carrier tunneling barrier across the interface.<sup>9,13</sup> On the moiré superlattice level, the low  $\rho$  and high  $\Phi$  at atop region indicate insufficient interfacial carriers and high tunneling barriers needed to be overcome for electron tunneling, both contributing to a poor contact quality and low interfacial conductance. On the atomic level, although  $\rho$  shows little difference between  $C_\alpha$  and  $C_\beta$  position, the tunneling barrier  $\Phi$  at  $C_\alpha$  position is much lower, whereas the interfacial charge transfer and orbital overlap between C and Ru atoms are enhanced (Figure S7), leading to a better contact quality and high interfacial conductance at  $C_\alpha$  position. Similarly, the tunneling barriers  $\Phi$  along a series of pathways through different C–Ru pairs were calculated as shown by the red dots in Figure 4c, which shows strong correlation with the C–Ru interatomic distances. On the basis of the above electronic structure analysis, a phenomenological model is proposed to describe in real-space the atomic-scale contact quality (ACQ), that is, contact conductance between 2D materials and substrates (metals or 2D materials) in terms of the individual atom–atom contact quality (the carrier tunneling probability along the interatomic electron transport pathways). The details of the model are described below.

As described above, the tunneling barrier  $\Phi$  plays a major role in determining the individual atom–atom contact conductance and is closely related to the interatomic distance ( $d$ ); the individual atom–atom contact conductance ( $G_{\text{atomic}}$ ) was calculated by a simplified model of carbon and ruthenium linear chain contact as shown in Figure 4a and Figure S8. The  $G_{\text{atomic}}-d$  relationship of individual C–Ru atom contact is found to be exponential (eq 1) as shown in Figure 4b utilizing DFT+NEGF calculations. Meanwhile, the relationship between the tunneling barrier and interatomic distance  $\Phi-d$  in the linear chain contact model is obtained in Figure 4c (black fitted curve), which shows high consistency with that calculated along various transport pathways through the graphene/Ru interface (red dots). By the same linear chain contact model, the  $G_{\text{atomic}}-d$  relationship between different types of pair atoms can also be calculated as shown in Figure S8 and Table S1.

$$G_{\text{atomic}}(d_{\text{C-Ru}}) = e^{-3.49d_{\text{C-Ru}}+9.34} \quad (1)$$

By utilizing the  $G_{\text{atomic}}-d$  relationship calculated by linear chain contact model, the total interfacial conductance between 2D materials and substrate can be simply estimated by the pairwise summation of the individual atom–atom contact conductance along all possible electron transport pathways (eq 2), as shown in Figure 4d (white background area), as the many-body effect is found to play a relatively insignificant role (Figures S9 and S10 and Supplementary Discussion 3 and 4 in Supporting Information) and neglected. Here,  $m$  and  $n$  represent the total numbers of the Ru (top layer) and C atoms, respectively. Because the atom–atom contact conductance decreases exponentially with interatomic distance, a certain cutoff distance (5 Å) is adopted for the summation.

$$G_{\text{interface}} = \sum_{j=1}^n \sum_{i=1}^m G_{\text{atomic}}(d_{\text{C}_j\text{-Ru}_i}) = \sum_{j=1}^n \sum_{i=1}^m e^{-3.49d_{\text{C}_j\text{-Ru}_i}+9.34} \quad (2)$$

Besides the graphene/Ru interface, this formula can be adopted to calculate the contact conductance of various 2D materials/metal interfaces (Figure S11 and Supplementary Discussion 5 in Supporting Information), and the results are consistent with previous literatures.<sup>13,38</sup> The model and eq 2 were also adopted to demonstrate the enhancement of MoS<sub>2</sub>/Ti contact conductivity through improving the atomic-scale contact quality, by S-vacancies-induced surface reconstruction (Figure S12 and Supplementary Discussion 6 in Supporting Information).

The model is further used to simulate our c-AFM current map by considering the circuit containing both conductive tip/graphene and graphene/Ru interfaces, as shown in Figure 4d. For simplification, electron diffusion within the graphene plane is neglected, as graphene/metal interfacial electron transport is nearly ballistic with high transfer efficiency when subjected to an electric field along the surface normal direction,<sup>14</sup> which is the case in the present c-AFM setup (Figure 1a) and confirmed by our NEGF calculation (Figure S13 and Supplementary Discussion 7 in Supporting Information). Because intercalation is widely applied for regulating the electronic and magnetic properties of graphene,<sup>39–41</sup> we also confirmed the validity of this assumption in the systems with metal atoms as intercalating layers<sup>41</sup> (Figure S13). Therefore, the spatial distribution of the conductance  $G(x,y)$  can be expressed by the summation of graphene/Ru interfacial conductance  $G_{\text{interface}}(x,y)$  and Pt tip/graphene contact conductance  $G_{\text{surface}}(x,y)$ . The tip/graphene contact conductance  $G_{\text{surface}}(x,y)$  was modified to consider the effect of surface electron density variation ( $\rho_{\text{surface}}(x,y)$ ) induced by the Ru substrate, according to the Tersoff-Hamann theory<sup>42</sup>

$$G_{\text{surface}}(x,y) = \sum_{j=1}^{n'} (\rho_{\text{surface}-j}(x,y) \cdot e^{-3.91d_{\text{C}_j\text{-Pt}}(x,y)+A}) \quad (3)$$

The details of the  $G_{\text{surface}}(x,y)$  calculation is in Figure S14 and Supplementary Discussion 8 in Supporting Information. Finally, the equation for the local conductance at the c-AFM tip position  $G(x,y)$  is

$$G(x,y) = (G_{\text{surface}}^{-1}(x,y) + G_{\text{interface}}^{-1}(x,y))^{-1} \\ = \sum_{j=1}^{n'} \left( \rho_{\text{surface}-j}(x,y) \cdot e^{-3.91d_{\text{C}_j\text{-Pt}}(x,y)+A} \right)^{-1} \\ + \left( \sum_{i=1}^{m'} e^{-3.49d_{\text{C}_j\text{-Ru}_i}(x,y)+9.34} \right)^{-1} \quad (4)$$

where  $n'$  represents the number of C atoms nearby the tip position  $(x,y)$ , and  $m'$  represents the number of Ru atoms (top layer) adjacent to each of the  $n'$  carbon atoms. Although eq 2 calculates total conductance, eq 4 deals with the local contact conductance at the atomic level. The simulated c-AFM local conductance map by eq 4 is shown in Figure 4e, which captures the main features of c-AFM current image in Figure 1b,d), that is, “dark” regions correspond to the less conductive atop regions and the atomic-scale contrast of  $C_\alpha$  and  $C_\beta$  positions in fcc regions is well reproduced (local enlargements of Figure 4e).

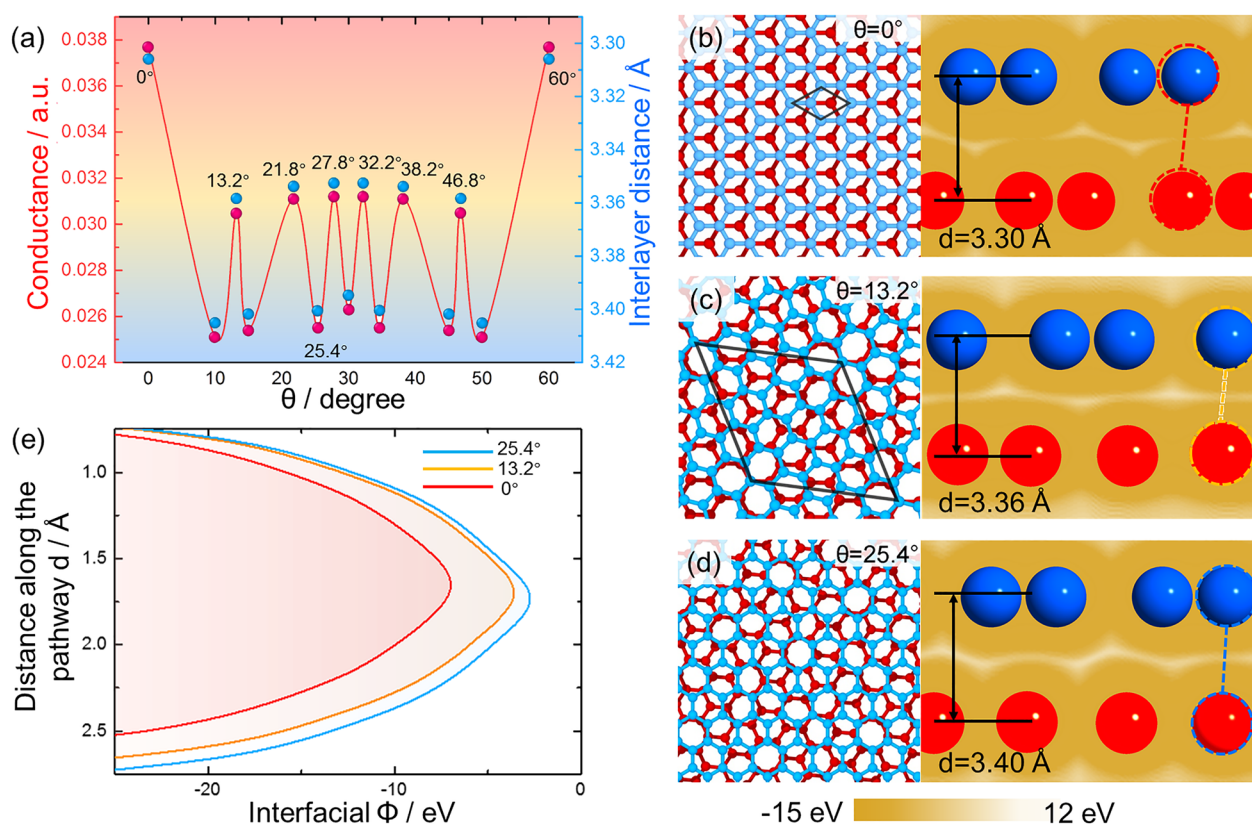


**Figure 5.** Understanding the angular dependence of the twisted bilayer graphene interfacial conductance from the perspective of atom–atom contact quality. (a) The interlayer conductance calculated by our model and averaged interlayer distance of bilayer graphene with a series of rotation angles  $\theta = 0^\circ, 10^\circ, 13.2^\circ, 15^\circ, 21.8^\circ, 25.4^\circ, 27.8^\circ, 30^\circ, 32.2^\circ, 34.6^\circ, 38.2^\circ, 45^\circ, 46.8^\circ, 50^\circ,$  and  $60^\circ$ . (b–d) Left: Atomic configurations of bilayer graphene with interlayer rotation angle  $\theta = 0^\circ, 13.2^\circ,$  and  $25.4^\circ$ . The superlattice of commensurate superstructures was marked by the black lines. Right: Electrostatic potential ( $\Phi$ ) distribution in the plane normal to the interfaces of corresponding atomic configurations. (e) The line profiles of  $\Phi$  along the electronic transport pathways indicated by the dashed lines in (b–d).

As the normal load applied by the AFM tip will initiate the out-of-plane deformation of graphene, we have discussed this effect on electrical conductance (more details in Supplementary Discussion 9 in Supporting Information). A 10-Pt-atom tip was utilized to indent toward graphene/Ru supercell at  $C_w$ ,  $C_\beta$ , and atop sites; the tip–graphene distances were set to be 2.0, 1.9, and 1.7 Å, respectively, to simulate the deformation of graphene/Ru(0001) interface under different contact loads. The morphologies of deformed graphene sheets are shown in Figure 4f (atop site) and Figure S15a–c ( $C_w$ ,  $C_\beta$  sites). The maximum normal force applied on the tip apex atom is 1.38 nN, corresponding to a local contact pressure of roughly 10 GPa. This suggests that the graphene structure can withstand the compression by the tip. The impact of deformations on electrical conductance is investigated using our ACQ model (eq 4), as shown in Figure 4g. The local conductance  $G$  at  $C_w$ ,  $C_\beta$ , and atop sites will increase with the indentation depth/contact load (Figure S15f), and the comparison of  $G$  is maintained as  $G_{\text{atop}} < G_{C_\beta} < G_{C_w}$  showing consistency with the trend of electrostatic barriers (Figure S15d,e) and the experiment results (Figure S16).

Besides the 2D materials/metal interfaces, the model can also be applied to the 2D/2D material interfaces. It has been used to capture the rotation angle-dependent interlayer conductance between misoriented graphene layers, which has aroused wide interest recently.<sup>10,43–46</sup> By using eq 2 of our real-space model and DFT optimized configurations (Figure S17), twist angle dependence of interlayer conductance in

bilayer graphene was calculated with rather low computational cost. As shown in Figure 5a, the conductance reaches the maximum at  $\theta = 0^\circ$  (and  $60^\circ$  due to rotation symmetry), whereas pronounced conductance peaks were also found at  $\theta = 13.2^\circ, 21.8^\circ, 27.8^\circ (32.2^\circ, 38.2^\circ, 46.8^\circ)$  corresponding to commensurate superstructures which are in good agreement with previous literatures.<sup>44</sup> This dependency has been quantified by a global registry index (GRI) model considering in-plane projected overlapping electron clouds between the C atoms in adjacent layers.<sup>43</sup> We show that the variation of interlayer conductance is also closely correlated to the variation of interlayer distance of bilayer graphene in “out-of-plane” direction (Figure 5a). At commensurate angles, both the decreasing interlayer distance and increasing GRI collectively contribute to the stronger C–C  $p_z$  orbital overlapping. Furthermore, the interfacial tunneling barriers along the transport pathways (dashed lines in Figure 5b–d) decrease at commensurate angles (Figure 5e), indicating better atom–atom contact quality between the C atoms in adjacent layers. On the contrary, the graphene layers become decoupled at incommensurate angles, accompanied by the degradation of atom–atom contact quality and interlayer conductance. Our calculation also shows that the commensurate  $\text{WSe}_2/\text{NbSe}_2$  interface has better electrical conductivity than the  $\text{WSe}_2/\text{Ti}$  interface (Figure S18) that is consistent with the recent research which suggests that 2D  $\text{NbSe}_2$  is superior to conventional 3D metals as a contact material.<sup>47,48</sup> We assume

that this model is also suitable for other situations where electron tunneling dominates the interfacial transport.

In summary, our atomic resolution conductance mapping and first-principles calculations have demonstrated that the local contact conductance of graphene/Ru interface is dominated by the individual atom–atom contact conductance along the electron transport pathways. On the basis of this concept, we have presented a real-space electrical contact model, which directly reveals the relationship between atomic contact structure and electrical contact quality of 2D interfaces for the first time. In addition to unraveling the atomic-level spatial modulation of graphene/Ru contact conductance, this model can also be applied to various kinds of 2D material/metal interfaces and 2D/2D material interfaces, which provide theoretical guidance for designing and tuning the interfacial electrical contact on the atomic-scale.

**Materials and Methods.** *Fabrication of Graphene/Ru(0001) Sample.* Chemical vapor deposition was utilized to fabricate the graphene/Ru(0001) sample. The single crystal Ru sample was cleaned by Ar ion sputtering for several cycles and confirmed clean by low energy electron diffraction (LEED) before the growth of graphene. Then the Ru(0001) substrate was exposed to ethylene with partial pressure  $1.4 \times 10^{-4}$  Pa at 850 °C for 100 s and graphene formed by the thermal decomposition of ethylene. The quality of graphene was checked by LEED after cooling down, and the sample showed clear diffraction spots of graphene/Ru(0001) moiré patterns.<sup>49</sup>

*Local Conductance Measurement.* The local current maps were obtained by Cypher c-AFM contact mode, made by Oxford Instruments, under atmospheric environment and 25 °C temperature. An Ir–Pt-coated AFM tip (SCM-PIT, tip radius  $R \sim 20$  nm, force constant  $k = 2.8$  N·m<sup>-1</sup>) was used to obtain the local current map. The normal load was set to 1000 nN (sliding speed = 0.59  $\mu$ m/s), a relatively high value to ensure good contact between tip and graphene. With the increase of c-AFM measurement time, tip wear is unavoidable and the current map becomes unstable. The stability and clearness of the current map is a prerequisite in our c-AFM measurement (Figure S21 and Supplementary Discussion 10 in Supporting Information). Bias voltage was set to 1, 20, and 30 mV to obtain local current map.

*Ab Initio Calculation Details.* The geometry optimization, charge density, difference charge density, partial charge density (carriers density), and electrostatic potential calculation of graphene/Ru(0001) interface was implemented in the Vienna ab initio Simulation Package (VASP). The calculation models are shown in Figure S5a. The projector-augmented-wave (PAW) method was utilized to model the core electrons. The optB86b-vdW exchange–correlation functional was utilized to approximately describe the dispersion interaction (van der Waals forces). The plane wave basis kinetic energy cut off was set to 400 eV. The graphene and first Ru(0001) layer were allowed to relax until the forces on all the relaxed atoms were less than 0.02 eV/Å. The transmission spectra,  $I$ – $V$  curves and transmission eigenstates calculations were implemented in the Atomistix ToolKit. The PAW pseudopotential type and general gradient approximate exchange–correlation functional was used. The real space mesh cutoff of 75 Ha was used for calculation. The calculation models are shown in Figure S5b–d. The electrodes were all set at a distance of 2.7 Å from the surface atoms to eliminate the changes of contact resistance between electrodes and surfaces.

*Derivation of the Interfacial Conductance Model.* Details are available in Figures S9, S10, S13, and S14 and the related discussions in Supporting Information.

## ■ ASSOCIATED CONTENT

### § Supporting Information

The Supporting Information is available free of charge on the ACS Publications website at DOI: 10.1021/acs.nanolett.9b00695.

Morphology and current maps of graphene/Ru(0001) at various bias voltages, comparison of imaging mechanisms and experimental results between c-AFM and STM, original experimental images, atomistic structures used in ab initio calculations, LDOS and difference charge density of graphene/Ru(0001), individual atom–atom contact conductance relationships for various atom pairs, discussions about many-body effect, pristine (or defective) MoS<sub>2</sub> (or graphene)/metal and WSe<sub>2</sub>/NbSe<sub>2</sub> interfacial conductance calculated by our model, the distribution of current in real space calculated by NEGF +DFT, details of calculating  $G_{\text{interface}}$  and calculated/experimental  $I$ – $V$  curves of graphene/Ru system (PDF)

## ■ AUTHOR INFORMATION

### Corresponding Author

\*E-mail: mtb@mail.tsinghua.edu.cn.

### ORCID

Lei Gao: 0000-0001-8555-5168

Qunyang Li: 0000-0002-6865-3863

Shixuan Du: 0000-0001-9323-1307

Xin Li: 0000-0002-4743-5509

Hong-Jun Gao: 0000-0002-6766-0623

Jianbin Luo: 0000-0002-5132-0712

Tian-Bao Ma: 0000-0001-8016-9241

### Author Contributions

T.M. conceived the project. A.S. and L.G. carried out the first-principles calculations. R.S. performed the c-AFM experiments. A.S. and T.M. developed the model. H.L., H.G., and S.D. prepared the samples. A.S. and T.M. wrote the manuscript. All authors analyzed and discussed the results and approved the manuscript.

### Notes

The authors declare no competing financial interest.

## ■ ACKNOWLEDGMENTS

The authors would like to acknowledge the support of the National Natural Science Foundation of China (Grants 51527901, 61390501, 11772169, 61504149, 51705017, and 11890671). Computations were conducted on the “Explorer 100” cluster system of the Tsinghua National Laboratory for Information Science and Technology.

## ■ REFERENCES

- (1) Allain, A.; Kang, J.; Banerjee, K.; Kis, A. Electrical contacts to two-dimensional semiconductors. *Nat. Mater.* **2015**, *14* (12), 1195–1205.
- (2) Schwierz, F. Graphene transistors. *Nat. Nanotechnol.* **2010**, *5* (7), 487–496.
- (3) Holm, R. *Electric Contacts*, 4th ed.; Springer-Verlag: Berlin, 1967.
- (4) Greenwood, J. A. Constriction resistance and real area of contact. *Br. J. Appl. Phys.* **1966**, *17* (12), 1621–1632.

- (5) Gotsmann, B.; Lantz, M. A. Quantized thermal transport across contacts of rough surfaces. *Nat. Mater.* **2013**, *12* (1), 59–65.
- (6) Krans, J. M.; Vanruijtenbeek, J. M.; Fisun, V. V.; Yanson, I. K.; Dejongh, L. J. The signature of conductance quantization in metallic contacts. *Nature* **1995**, *375* (6534), 767–769.
- (7) Sharvin, Y. V. A possible method for studying Fermi surfaces. *Sov. Phys.-JETP* **1965**, *21* (3), 655–656.
- (8) Agrait, N. Quantum properties of atomic-sized conductors. *Phys. Rep.* **2003**, *377* (2–3), 81–279.
- (9) Popov, I.; Seifert, G.; Tomanek, D. Designing electrical contacts to MoS<sub>2</sub> monolayers: a computational study. *Phys. Rev. Lett.* **2012**, *108* (15), 156802.
- (10) Chari, T.; Ribeiro-Palau, R.; Dean, C. R.; Shepard, K. Resistivity of Rotated Graphite-Graphene Contacts. *Nano Lett.* **2016**, *16* (7), 4477–4482.
- (11) Xu, Y.; Cheng, C.; Du, S.; Yang, J.; Yu, B.; Luo, J.; et al. Contacts between Two- and Three-Dimensional Materials: Ohmic, Schottky, and p-n Heterojunctions. *ACS Nano* **2016**, *10* (5), 4895–4919.
- (12) Tomanek, D. Interfacing graphene and related 2D materials with the 3D world. *J. Phys.: Condens. Matter* **2015**, *27* (13), 133203.
- (13) Kang, J.; Liu, W.; Sarkar, D.; Jena, D.; Banerjee, K. Computational Study of Metal Contacts to Monolayer Transition-Metal Dichalcogenide Semiconductors. *Phys. Rev. X* **2014**, *4* (3), 031005.
- (14) Xia, F.; Perebeinos, V.; Lin, Y. M.; Wu, Y.; Avouris, P. The origin and limits of metal-graphene junction resistance. *Nat. Nanotechnol.* **2011**, *6* (3), 179–184.
- (15) Landauer, R. Electrical resistance of disordered one-dimensional lattices. *Philos. Mag.* **1970**, *21* (172), 863–867.
- (16) Liao, M.; Wu, Z. W.; Du, L.; Zhang, T.; Wei, Z.; Zhu, J.; et al. Twist angle-dependent conductivities across MoS<sub>2</sub>/graphene heterojunctions. *Nat. Commun.* **2018**, *9* (1), 4068.
- (17) Somvanshi, D.; Kallatt, S.; Venkatesh, C.; Nair, S.; Gupta, G.; Anthony, J. K.; et al. Nature of carrier injection in metal/2D-semiconductor interface and its implications for the limits of contact resistance. *Phys. Rev. B: Condens. Matter Mater. Phys.* **2017**, *96* (20), 205423.
- (18) Crowell, C. The Richardson constant for thermionic emission in Schottky barrier diodes. *Solid-State Electron.* **1965**, *8* (4), 395–399.
- (19) Wang, L.; Meric, I.; Huang, P. Y.; Gao, Q.; Gao, Y.; Tran, H.; et al. One-dimensional electrical contact to a two-dimensional material. *Science* **2013**, *342* (6158), 614–617.
- (20) Park, H. Y.; Jung, W. S.; Kang, D. H.; Jeon, J.; Yoo, G.; Park, Y.; et al. Extremely Low Contact Resistance on Graphene through n-Type Doping and Edge Contact Design. *Adv. Mater.* **2016**, *28* (5), 864–870.
- (21) Chuang, H. J.; Chamlagain, B.; Koehler, M.; Perera, M. M.; Yan, J.; Mandrus, D.; et al. Low-Resistance 2D/2D Ohmic Contacts: A Universal Approach to High-Performance WSe<sub>2</sub>, MoS<sub>2</sub>, and MoSe<sub>2</sub> Transistors. *Nano Lett.* **2016**, *16* (3), 1896–1902.
- (22) Liu, W.; Kang, J.; Sarkar, D.; Khatami, Y.; Jena, D.; Banerjee, K. Role of metal contacts in designing high-performance monolayer n-type WSe<sub>2</sub> field effect transistors. *Nano Lett.* **2013**, *13* (5), 1983–1990.
- (23) Lee, G.-H.; Yu, Y.-J.; Lee, C.; Dean, C.; Shepard, K. L.; Kim, P.; et al. Electron tunneling through atomically flat and ultrathin hexagonal boron nitride. *Appl. Phys. Lett.* **2011**, *99* (24), 243114.
- (24) Zhang, L. Z.; Du, S. X.; Sun, J. T.; Huang, L.; Meng, L.; Xu, W. Y.; et al. Growth Mechanism of Metal Clusters on a Graphene/Ru(0001) Template. *Adv. Mater. Interfaces* **2014**, *1* (3), 1300104.
- (25) Altenburg, S.; Kröger, J.; Wang, B.; Bocquet, M.-L.; Lorente, N.; Berndt, R. Graphene on Ru (0001): contact formation and chemical reactivity on the atomic scale. *Phys. Rev. Lett.* **2010**, *105* (23), 236101.
- (26) Marchini, S.; Günther, S.; Wintterlin, J. Scanning tunneling microscopy of graphene on Ru (0001). *Phys. Rev. B: Condens. Matter Mater. Phys.* **2007**, *76* (7), 075429.
- (27) Voloshina, E. N.; Fertitta, E.; Garhofer, A.; Mittendorfer, F.; Fonin, M.; Thissen, A.; et al. Electronic structure and imaging contrast of graphene moire on metals. *Sci. Rep.* **2013**, *3*, 1072.
- (28) Wang, B.; Bocquet, M.-L.; Marchini, S.; Günther, S.; Wintterlin, J. Chemical origin of a graphene moiré overlayer on Ru (0001). *Phys. Chem. Chem. Phys.* **2008**, *10* (24), 3530–3534.
- (29) Li, S.; Li, Q.; Carpick, R. W.; Gumbsch, P.; Liu, X. Z.; Ding, X.; et al. The evolving quality of frictional contact with graphene. *Nature* **2016**, *539* (7630), 541–545.
- (30) Li, Q.; Tullis, T. E.; Goldsby, D.; Carpick, R. W. Frictional ageing from interfacial bonding and the origins of rate and state friction. *Nature* **2011**, *480* (7376), 233–236.
- (31) Lee, C.; Li, Q. Y.; Kalb, W.; Liu, X. Z.; Berger, H.; Carpick, R. W.; et al. Frictional Characteristics of Atomically Thin Sheets. *Science* **2010**, *328* (5974), 76–80.
- (32) Lanza, M.; Porti, M.; Nafria, M.; Aymerich, X.; Whittaker, E.; Hamilton, B. Note: Electrical resolution during conductive atomic force microscopy measurements under different environmental conditions and contact forces. *Rev. Sci. Instrum.* **2010**, *81* (10), 106110.
- (33) Balog, R.; Jorgensen, B.; Nilsson, L.; Andersen, M.; Rienks, E.; Bianchi, M.; et al. Bandgap opening in graphene induced by patterned hydrogen adsorption. *Nat. Mater.* **2010**, *9* (4), 315–319.
- (34) Zhang, J.; Shen, G.; Wang, W.; Zhou, X.; Guo, S. Individual nanocomposite sheets of chemically reduced graphene oxide and poly(N-vinyl pyrrolidone): preparation and humidity sensing characteristics. *J. Mater. Chem.* **2010**, *20* (48), 10824.
- (35) Atomistix ToolKit version 16.4; QuantumWise A/S, [www.quantumwise.com](http://www.quantumwise.com) (accessed on May 16, 2019).
- (36) Brandbyge, M.; Mozos, J. L.; Ordejon, P.; Taylor, J.; Stokbro, K. Density-functional method for nonequilibrium electron transport. *Phys. Rev. B: Condens. Matter Mater. Phys.* **2002**, *65* (16), 165401.
- (37) Lin, H. P.; Rauba, J. M. C.; Thygesen, K. S.; Jacobsen, K. W.; Simmons, M. Y.; Hofer, W. A. First-principles modelling of scanning tunneling microscopy using non-equilibrium Green's functions. *Frontiers of Physics in China* **2010**, *5* (4), 369–379.
- (38) Ran, Q.; Gao, M.; Guan, X.; Wang, Y.; Yu, Z. First-principles investigation on bonding formation and electronic structure of metal-graphene contacts. *Appl. Phys. Lett.* **2009**, *94* (10), 103511.
- (39) Dedkov, Y.; Voloshina, E. Spectroscopic and DFT studies of graphene intercalation systems on metals. *J. Electron Spectrosc. Relat. Phenom.* **2017**, *219*, 77–85.
- (40) Sicot, M.; Leicht, P.; Zusan, A.; Bouvron, S.; Zander, O.; Weser, M.; et al. Size-Selected Epitaxial Nanoislands Underneath Graphene Moire on Rh(111). *ACS Nano* **2012**, *6* (1), 151–158.
- (41) Weser, M.; Voloshina, E. N.; Horn, K.; Dedkov, Y. S. Electronic structure and magnetic properties of the graphene/Fe/Ni111 intercalation-like system. *Phys. Chem. Chem. Phys.* **2011**, *13* (16), 7534–7539.
- (42) Hofer, W. A.; Foster, A. S.; Shluger, A. L. Theories of scanning probe microscopes at the atomic scale. *Rev. Mod. Phys.* **2003**, *75* (4), 1287–1331.
- (43) Koren, E.; Leven, I.; Lörtscher, E.; Knoll, A.; Hod, O.; Duerig, U. Coherent commensurate electronic states at the interface between misoriented graphene layers. *Nat. Nanotechnol.* **2016**, *11* (9), 752.
- (44) Bistrizter, R.; MacDonald, A. H. Transport between twisted graphene layers. *Phys. Rev. B: Condens. Matter Mater. Phys.* **2010**, *81* (24), 245412.
- (45) Cao, Y.; Fatemi, V.; Fang, S.; Watanabe, K.; Taniguchi, T.; Kaxiras, E.; et al. Unconventional superconductivity in magic-angle graphene superlattices. *Nature* **2018**, *556* (7699), 43–50.
- (46) Yoo, H.; Engelke, R.; Carr, S.; Fang, S.; Zhang, K.; Cazeaux, P.; Kim, P.; et al. Atomic and electronic reconstruction at the van der Waals interface in twisted bilayer graphene. *Nat. Mater.* **2019**, *18* (5), 448–453.
- (47) Guan, J.; Chuang, H. J.; Zhou, Z.; Tomanek, D. Optimizing Charge Injection across Transition Metal Dichalcogenide Heterojunctions: Theory and Experiment. *ACS Nano* **2017**, *11* (4), 3904–3910.

(48) Chuang, H. J.; Chamlagain, B.; Koehler, M.; Perera, M. M.; Yan, J.; Mandrus, D.; et al. Low-Resistance 2D/2D Ohmic Contacts: A Universal Approach to High-Performance WSe<sub>2</sub>, MoS<sub>2</sub>, and MoSe<sub>2</sub> Transistors. *Nano Lett.* **2016**, *16* (3), 1896–1902.

(49) Pan, Y.; Zhang, H.; Shi, D.; Sun, J.; Du, S.; Liu, F.; et al. Highly ordered, millimeter-scale, continuous, single-crystalline graphene monolayer formed on Ru (0001). *Adv. Mater.* **2009**, *21* (27), 2777–2780.